AIMS Energy, 11(6): 1211–1230.
DOI: 10.3934/energy.2023055
Received: 02 August 2023
Revised: 16 October 2023
Accepted: 01 November 2023
Published: 23 November 2023

http://www.aimspress.com/journal/energy

Research article

Numerical investigation and improvement of the aerodynamic performance of a modified elliptical-bladed Savonius-style wind turbine

Sri Kurniati[1,*], Sudirman Syam[1] and Arifin Sanusi[2]

[1] Department of Electrical Engineering, Faculty of Science and Technology, Nusa Cendana University, Kupang-NTT, 85228, Indonesia
[2] Department of Mechanical Engineering, Faculty of Science and Technology, Nusa Cendana University, Jl. Adisucipto, Penfui-Kupang-NTT, 85228, Indonesia

* **Correspondence:** Email: sri_kurniati@staf.undana.ac.id; Tel: +628123744422.

Abstract: The Savonius turbine has an advantage over other types of vertical axis wind turbines (VAWT), which have speeds ranging from the lowest wind speed to the highest. However, the main problem is the negative torque on the rotary blades. This paper used computational fluid dynamics to numerically investigate the two-dimensional flow analysis of a modified elliptical Savonius wind turbine. This study investigated and compared five rotor blades: Classic, elliptical, and their three modifications. The behavior of wind energy was studied explicitly by changing the angle of the axis of the elliptical blade from the concave side, which leads to a convex shape to increase the area affected by the thrust force and increase the positive torque. The ANSYS (previously known as STASYS Structural Analysis System) Fluent version 15 software solves the unstable Reynolds-Naiver-Stokes (URAN) equation. The coupling algorithm solves the pressure-based coupling pressure velocity using the ANSYS Fluent. In the simulation, the drag, lift, and moment coefficients on the Savonius turbine were calculated directly at each change in the axis angle. The test results at wind speeds of up to nine m/s showed that the modified elliptical turbine with an axis angle of 50° had the highest coefficient power (Cp) among other elliptical blade modifications. In comparison, the test results with variations in wind speeds of 4–12 m/s showed that turbines with an axis angle of 55° performed better with a higher tip speed ratio (TSR) than other models.

Keywords: wind energy; computational fluid; blade angle; power coefficient

1. Introduction

The Savonius wind turbine is a simple, semicircular vertical axis device mounted on opposite sides of the vertical axis (two blades). It operates by drag and cannot rotate faster than the wind speed [1]. In this case, the tip speed ratio (TSR) is equal to or less than one [2,3]. The Savonius wind turbine seems very promising for small-scale applications because of its easy installation, simple design, relatively low operating speed, good starting ability, insensitivity to wind direction, and low cost. Although significant progress has been made in wind turbine design, more than the available technical designs are needed to develop reliable wind energy conversion specifically aimed at small-scale applications. Some researchers report lower efficiency compared to other wind turbines. The working principle of the Savonius turbine is based on the difference in drag force between the convex part and the concave part of the rotor blade; the blade rotates on a vertical axis. According to [4], the main driving force in the Savonius rotor is the drag force. Other researchers explained the concept of Savonius turbine drag force by carrying out dynamic analysis to determine the effect of lift force. As a result, turbine efficiency is influenced by drag force and lift force [5–7]. In [8], the weakness of the Savonius turbine was caused by the influence of turbine humidity forces; the efficiency was low. In addition, the number of blades greatly influences the rotor performance [9,10]. The paper [11] concludes that the Savonius turbine with two blades has a higher power coefficient and is more efficient under the same test conditions as the three blades.

Other parameters that influence the performance of Savonius turbines are geometric design [12–14], the influence of gap size [15] and aspect ratio [13]. In [16], an aspect ratio of 0.7 has the maximum CP, then a two-blade turbine with zero overlap performs better than one with three overlapping blades [11]. The overlaps and gaps between Savonius blades allow fluid to enter the concave side of the blade, then flow to the other side and create additional pressure. In addition, some researchers vary the rotor angle of the blade profile. The blade profile is an essential design for Savonius rotors. According to [17], varying the blade profile by changing the bend angle will significantly affect rotor performance. Differences in the configuration and arrangement of the Savonius rotor show that the twist angle influences rotor performance [18] and the straight blade angle [19]. That means, in general, the main geometric and flow parameters that influence the performance of a Savonius turbine are the blade profile, overlap ratio, aspect ratio and the Reynolds number (Re). However, among these parameters, blade profile significantly influences power production.

Besides that, recent studies show that elliptical blades can help harness more wind energy. It is known that the Savonius elliptical-bladed wind turbine produces relatively better performance than conventionally used semicircular-bladed turbines. In computational and experimental studies by [20], improved flow characteristics and better performance of elliptical-bladed turbines were obtained compared to conventional semicircular designs. That is mainly due to the lower tip loss and delayed flow separation, which allows elliptical turbines to obtain higher rotational speeds than semicircular turbines under a given wind load. In recent years, several research works have focused on improving the performance of the elliptical blade. The work [21] experimentally determined the optimal blade configuration involving chord length, turbine height, aspect ratio, and overlap ratio required to obtain the necessary power and torque from an elliptical-bladed Savonius wind turbine. Previously, paper [22]

also reported numerically that elliptical turbines have higher coefficients than conventional turbines. Later, Talukdar and Kulkarni [23] investigated the performance of a two-band elliptical turbine rotor for its dynamic torque and power characteristics.

Furthermore, researchers focused on improving the performance of the elliptical blade model, such as changing the angle to 50° concerning the horizontal axis by Banerjee [20]. In this investigation, the cross-sectional angle has not been optimized, which is likely why it does not get much of a performance boost over the semicircular design. Paper [24] tried to optimize this profile with numerical simulations. The elliptical blade profile was tested at different cutting angles, namely, θ = 45°, 47.5°, 50° and 55°, and the highest CP and power were obtained at an angle of 47.5°. However, in this research, testing was only carried out at certain wind speeds.

Therefore, this paper will focus on the numerical study of the Savonius turbine's elliptical type and its modification and comparison with conventional Savonius turbines at 5–12 m/s wind speeds. The aim was to test various elliptical blade angle shapes to obtain optimal geometry by looking for considerable momentum and power coefficients. In this test, we did not control wind speed changes, as done by Jiao et al. [25] and Meng et al. [26]. This research only focuses on changes in the CP and TSR values of the five types of turbines tested using a wind tunnel. Changes in wind speed are made simply by opening the wind cover input hole of the blower.

2. Theoretical approach to the fluid simulation model

This paper develops a flow model based on the approximate solution of the equations of motion, then the finite volume method uses the time-average continuity for the incompressible flow. The Cartesian coordinate system is shown in Eqs 1–4.

$$\frac{\partial u}{\partial t}+\frac{\partial uu}{\partial x}+\frac{\partial vu}{\partial y}+\frac{\partial wu}{\partial z} = -\frac{1}{\rho}\frac{\partial p}{\partial x}+\frac{1}{\rho}\frac{\partial t_{xx}}{\partial x}+\frac{1}{\rho}\frac{\partial u_{yx}}{\partial y}+\frac{1}{\rho}\frac{\partial u_{zx}}{\partial z}+g_x \quad (1)$$

$$\frac{\partial v}{\partial t}+\frac{\partial uv}{\partial x}+\frac{\partial vv}{\partial y}+\frac{\partial wv}{\partial z} = -\frac{1}{\rho}\frac{\partial p}{\partial y}+\frac{1}{\rho}\frac{\partial t_{xy}}{\partial x}+\frac{1}{\rho}\frac{\partial u_{yy}}{\partial y}+\frac{1}{\rho}\frac{\partial u_{zy}}{\partial z}+g_y \quad (2)$$

$$\frac{\partial w}{\partial t}+\frac{\partial uw}{\partial x}+\frac{\partial vw}{\partial y}+\frac{\partial ww}{\partial z} = -\frac{1}{\rho}\frac{\partial p}{\partial z}+\frac{1}{\rho}\frac{\partial t_{xz}}{\partial x}+\frac{1}{\rho}\frac{\partial u_{yz}}{\partial y}+\frac{1}{\rho}\frac{\partial u_{zz}}{\partial z}+g_z \quad (3)$$

$$\frac{\partial u}{\partial x}+\frac{\partial v}{\partial x}+\frac{\partial w}{\partial y} = 0 \quad (4)$$

where:

- x, y and z are cartesian coordinates on the horizontal, transverse, and vertical,
- u, v and w are the corresponding velocity (time average) components,
- p is the pressure (average time),
- ρ is the density of water,
- gx, gy and gz are the x, y, and z components of the acceleration due to gravity, and,
- ij is the j-direction component of the shear stress acting on the surface normal to the i-direction.

Molecular viscosities and turbulent fluctuations cause pressures. The viscous voltage is much smaller than the turbulence voltage for currents with high Reynolds values, so that it can be neglected. In the Boussinesq Eddy viscosity concept, the stress is proportional to the velocity gradient according to Eq 5.

$$\frac{r_{xx}}{\rho} = \boldsymbol{vt^2}\ \frac{\partial \boldsymbol{u}}{\partial \boldsymbol{x}} - \frac{\boldsymbol{2}}{\boldsymbol{3}}\boldsymbol{k} \quad \frac{r_{xy}}{\rho} = \frac{r_{yx}}{\rho} = \boldsymbol{vt}\left(\frac{\partial \boldsymbol{u}}{\partial \boldsymbol{x}} + \frac{\partial \boldsymbol{u}}{\partial \boldsymbol{y}}\right)$$

$$\frac{r_{yy}}{\rho} = \boldsymbol{vt^2}\ \frac{\partial \boldsymbol{v}}{\partial \boldsymbol{y}} - \frac{\boldsymbol{2}}{\boldsymbol{3}}\boldsymbol{k} \quad \frac{r_{xz}}{\rho} = \frac{r_{zx}}{\rho} = \boldsymbol{vt}\left(\frac{\partial \boldsymbol{w}}{\partial \boldsymbol{x}} + \frac{\partial \boldsymbol{u}}{\partial \boldsymbol{z}}\right)$$

$$\frac{r_{zz}}{\rho} = \boldsymbol{vt^2}\ \frac{\partial \boldsymbol{w}}{\partial \boldsymbol{z}} - \frac{\boldsymbol{2}}{\boldsymbol{3}}\boldsymbol{k} \quad \frac{r_{yz}}{\rho} = \frac{r_{zy}}{\rho} = \boldsymbol{vt}\left(\frac{\partial \boldsymbol{w}}{\partial \boldsymbol{y}} + \frac{\partial \boldsymbol{v}}{\partial \boldsymbol{z}}\right) \quad (5)$$

where:

- t is the turbulent or eddy viscosity and,
- k is turbulent kinetic energy defined as $\boldsymbol{k} = \frac{\boldsymbol{1}}{\boldsymbol{2}}(\overline{\boldsymbol{u'u'}} + \overline{\boldsymbol{v'v'}} + \overline{\boldsymbol{w'w'}}$ where the superscript symbol means the fluctuating component.

By including the definition in Eq 5 into the momentum equation, for Eqs 1–3, we get:

$$\frac{\partial u}{\partial t} + \frac{\partial uu}{\partial x} + \frac{\partial vu}{\partial y} + \frac{\partial wu}{\partial z} = -\frac{1}{\rho}\frac{\partial p}{\partial x} + \frac{2}{3}\frac{\partial k}{\partial x} + \frac{\partial}{\partial x}vt^2\left(\frac{\partial u}{\partial x}\right) + \frac{\partial}{\partial y}vt\left(\frac{\partial v}{\partial x} + \frac{\partial u}{\partial y}\right) + \frac{\partial}{\partial z}vt\left(\frac{\partial w}{\partial x} + \frac{\partial u}{\partial z}\right) + g_x \quad (6)$$

$$\frac{\partial v}{\partial t} + \frac{\partial uv}{\partial x} + \frac{\partial vv}{\partial y} + \frac{\partial wv}{\partial z} = -\frac{1}{\rho}\frac{\partial p}{\partial y} + \frac{2}{3}\frac{\partial k}{\partial y} + \frac{\partial}{\partial x}vt\left(\frac{\partial u}{\partial x} + \frac{\partial u}{\partial y}\right) + \frac{\partial}{\partial y}vt^2\left(\frac{\partial v}{\partial y}\right) + \frac{\partial}{\partial z}vt\left(\frac{\partial w}{\partial y} + \frac{\partial v}{\partial z}\right) + g_y \quad (7)$$

$$\frac{\partial w}{\partial t} + \frac{\partial uw}{\partial x} + \frac{\partial vw}{\partial y} + \frac{\partial ww}{\partial z} = -\frac{1}{\rho}\frac{\partial p}{\partial z} + \frac{2}{3}\frac{\partial k}{\partial z} + \frac{\partial}{\partial x}vt\left(\frac{\partial w}{\partial x} + \frac{\partial u}{\partial z}\right) + \frac{\partial}{\partial y}vt\left(\frac{\partial w}{\partial y} + \frac{\partial v}{\partial z}\right) + \frac{\partial}{\partial z}vt^2\left(\frac{\partial w}{\partial z}\right) + g_z \quad (8)$$

Separating the normal and second derivatives and placing the first on the left side, we get the equation:

$$\frac{\partial u}{\partial t} + \frac{\partial uu}{\partial x} + \frac{\partial vu}{\partial y} + \frac{\partial wu}{\partial z} - \frac{\partial}{\partial x}\left(vt\frac{\partial u}{\partial x}\right) - \frac{\partial}{\partial y}\left(vt\frac{\partial u}{\partial y}\right) - \frac{\partial}{\partial z}\left(vt\frac{\partial u}{\partial z}\right)$$

$$= -\frac{1}{\rho}\frac{\partial p}{\partial x} + \frac{\partial}{\partial x}\left(vt\ \frac{\partial u}{\partial x}\right) + \frac{\partial}{\partial y}\left(vt\frac{\partial v}{\partial x}\right) + \frac{\partial}{\partial z}\left(vt\frac{\partial w}{\partial x}\right) + g_x \quad (9)$$

$$\frac{\partial u}{\partial t} + \frac{\partial uv}{\partial x} + \frac{\partial vv}{\partial y} + \frac{\partial wu}{\partial z} - \frac{\partial}{\partial x}\left(vt\frac{\partial v}{\partial x}\right) - \frac{\partial}{\partial y}\left(vt\frac{\partial v}{\partial y}\right) - \frac{\partial}{\partial z}\left(vt\frac{\partial v}{\partial z}\right)$$

$$= -\frac{1}{\rho}\frac{\partial p}{\partial y} + \frac{\partial}{\partial x}\left(vt\ \frac{\partial u}{\partial y}\right) + \frac{\partial}{\partial y}\left(vt\frac{\partial v}{\partial y}\right) + \frac{\partial}{\partial z}\left(vt\frac{\partial w}{\partial y}\right) + g_y \quad (10)$$

$$\frac{\partial w}{\partial t} + \frac{\partial uw}{\partial x} + \frac{\partial vw}{\partial y} + \frac{\partial ww}{\partial z} - \frac{\partial}{\partial x}\left(vt\frac{\partial w}{\partial x}\right) - \frac{\partial}{\partial y}\left(vt\frac{\partial w}{\partial y}\right) - \frac{\partial}{\partial z}\left(vt\frac{\partial w}{\partial z}\right)$$

$$= -\frac{1}{\rho}\frac{\partial p}{\partial z} + \frac{\partial}{\partial x}\left(vt\ \frac{\partial u}{\partial z}\right) + \frac{\partial}{\partial y}\left(vt\frac{\partial v}{\partial z}\right) + \frac{\partial}{\partial z}\left(vt\frac{\partial w}{\partial z}\right) + g_z \quad (11)$$

The second to fourth terms on the left side of Eqs 9–11 represent convective transport, and the next three represent diffusion transport. The terms on the righthand side are taken as sources and treated as known quantities when solving the velocity components u, v and w equations. The kinetic turbulent energy gradient is slight compared to the pressure gradient, so the turbulent kinetic energy is neglected. From the turbulence model k-ε, turbulent viscosity, t, the results are:

$$\boldsymbol{v_t = c_\mu \rho \frac{k^2}{\varepsilon}} \tag{12}$$

where ε is turbulent kinetic energy dissipation.

The distribution field of turbulent kinetic energy and its dissipation is obtained from the transfer as follows:

$$\frac{\partial k}{\partial t} + \frac{\partial uk}{\partial x} + \frac{\partial vk}{\partial y} + \frac{\partial wk}{\partial z} - \frac{\partial}{\partial x}\left(\frac{vt}{\sigma k}\frac{\partial k}{\partial x}\right) - \frac{\partial}{\partial y}\left(\frac{vt}{\sigma k}\frac{\partial k}{\partial y}\right) - \frac{\partial}{\partial z}\left(\frac{vt}{\sigma k}\frac{\partial k}{\partial z}\right) = G - \varepsilon \tag{13}$$

$$\frac{\partial \varepsilon}{\partial t} + \frac{\partial u\varepsilon}{\partial x} + \frac{\partial v\varepsilon}{\partial y} + \frac{\partial w\varepsilon}{\partial z} - \frac{\partial}{\partial x}\left(\frac{vt}{\sigma \varepsilon}\frac{\partial \varepsilon}{\partial x}\right) - \frac{\partial}{\partial y}\left(\frac{vt}{\sigma \varepsilon}\frac{\partial \varepsilon}{\partial y}\right) - \frac{\partial}{\partial z}\left(\frac{vt}{\sigma \varepsilon}\frac{\partial \varepsilon}{\partial z}\right) = c_1 G - c_2 \varepsilon, \tag{14}$$

where G is the production of kinetic energy given from the equation:

$$G = vt\{2\left(\frac{\partial u}{\partial x}\right)^2 + \left(\frac{\partial u}{\partial y} + \frac{\partial v}{\partial x}\right)\frac{\partial u}{\partial y} + \left(\frac{\partial u}{\partial z} + \frac{\partial w}{\partial x}\right)\frac{\partial u}{\partial z} + \left(\frac{\partial v}{\partial x} + \frac{\partial u}{\partial y}\right)\frac{\partial v}{\partial x} + 2\left(\frac{\partial v}{\partial y}\right)^2 + \left(\frac{\partial v}{\partial z} + \frac{\partial w}{\partial y}\right)\frac{\partial v}{\partial z} + \left(\frac{\partial w}{\partial x} + \frac{\partial u}{\partial z}\right)\frac{\partial w}{\partial x} + \left(\frac{\partial w}{\partial y} + \frac{\partial v}{\partial z}\right)\frac{\partial w}{\partial y} + 2\left(\frac{\partial w}{\partial z}\right)^2\} \tag{15}$$

The model coefficients c, c_1, c_2 and k and the transport equation above are assumed to be constant with the values in Table 1. The model coefficients are obtained from experiments and evolve over time. The most widely accepted values currently come from Launder and Sharma [27] as follows:

Table 1. Coefficient values in the k-epsilon model.

c_μ	c_1	c_2	σ_k	σ_ε
0.09	1.44	1.92	1.0	1.3

To further facilitate continuity, Eq 4, the momentum equation, Eqs 9–11, transport equation of k and Eqs 13 and 14 are converted to the general transfer equation:

$$s\frac{\partial \phi_\ell}{\partial t} + \nabla\left(\emptyset_\ell \vec{V}\right) - \nabla\left(\Gamma_\ell \vec{V} \emptyset_\ell\right) = R_\ell \tag{16}$$

where:

- $\boldsymbol{\Phi}$ is a dependent scalar variable,
- $\vec{\boldsymbol{V}}$ is the velocity vector,
- $\boldsymbol{\Gamma_P}$ is the diffusion coefficient and
- $\boldsymbol{R_\ell}$ is a scalar source column matrix.

Table 2. The terms in the equation of public transport, Eq 16.

$$s\frac{\partial \phi_\ell}{\partial t} + \nabla\left(\emptyset_\ell \vec{V}\right) - \nabla\left(\Gamma_\ell \vec{V} \emptyset_\ell\right) = R_\ell \tag{16}$$

l	$\emptyset_\ell$	Γ_ℓ	
1	U	vt	$-\frac{1}{\rho}\frac{\partial \rho}{\partial x} + \frac{\partial}{\partial x}\left(vt\frac{\partial u}{\partial x}\right) + \frac{\partial}{\partial y}\left(vt\frac{\partial v}{\partial x}\right) + \frac{\partial}{\partial z}\left(vt\frac{\partial w}{\partial x}\right) + gx$
2	V	vt	$-\frac{1}{\rho}\frac{\partial \rho}{\partial y} + \frac{\partial}{\partial x}\left(vt\frac{\partial u}{\partial y}\right) + \frac{\partial}{\partial y}\left(vt\frac{\partial v}{\partial y}\right) + \frac{\partial}{\partial z}\left(vt\frac{\partial w}{\partial y}\right) + gy$
3	W	vt	$-\frac{1}{\rho}\frac{\partial \rho}{\partial z} + \frac{\partial}{\partial x}\left(vt\frac{\partial u}{\partial z}\right) + \frac{\partial}{\partial y}\left(vt\frac{\partial v}{\partial z}\right) + \frac{\partial}{\partial z}\left(vt\frac{\partial w}{\partial z}\right) + gz$
4	1	0	0
5	K	$vt/$	$G - \varepsilon$
6	ε	$vt/$	$C_1\frac{\varepsilon}{k}G - c_2\frac{\varepsilon}{k}\varepsilon$

Integrate this equation in the discrete volume method of the 3D result:

$$\frac{\partial}{\partial t}\iiint_\forall \boldsymbol{\phi_\ell} d\forall + \iiint_\forall \nabla\left(\boldsymbol{\phi_\ell} d\vec{V}\right)\mathbf{d}\forall - \iiint_\forall \nabla\left(\boldsymbol{\Gamma_\ell}\vec{\nabla}\boldsymbol{\phi_\ell}\right)\mathbf{d}\forall = \iiint_\forall \mathbf{R_\ell}\,\mathbf{d}\forall \tag{17}$$

The volume integrals of the convective and diffusion terms, the second and third terms on the left, can be expressed as integrals over a closed surface constraining control of volume by applying Gauss's divergence theorem:

$$\frac{\partial}{\partial t}\iiint_\forall \phi_\ell d\forall + \oiint_s \phi_\ell \vec{V}.d\vec{S} - \oiint_s \Gamma_\ell \vec{V}\phi_\ell.d\vec{S} = \iiint_\forall \mathrm{R}_\ell d\forall \tag{18}$$

where S is the surface normal vector to the control volume $d\forall$.

3. Materials and methods

3.1. Geometry details

This research focuses on modifying the geometry of the Elliptical-type Savonius windmill, especially on the variation of the blade axis angle. As a basic model, the Elliptical type Savonius turbine as Banerjee designed it [20]. 2D simulations were also done to compare semicircular or classic blade profiles directly. The classical geometry of the turbine to be tested is shown in Figure 1. A conventional Savonius blade with a diameter (d) 9.5 mm, endplate diameter (De) 200 mm, rotor diameter (D) 117 mm 1, overlap distance and (e) 20 mm, a shaft diameter of 10 mm. In this case, the simulation domain has two main zones: The inner domain and the outer domain. The inner domain is a circular domain that rotates and is adjacent to the turbine to simulate the rotor mechanism and its angle changes with time.

In the modified geometry, the basic axis angle of 40° elliptical-type turbines is illustrated in Figure 2(a). The diameter of the rotor, end-plate and the thickness of the blade remain the same, while at the blade's tip, a change in the axis angle is introduced. Changes in the base axis angle were made by varying the blade axis angle from 45°, 50° and 55° (Figure 2(b)–(d)). Here, a numerical study or computational fluid dynamics (CFD) investigates four elliptical models and one conventional type.

CFD is a numerical calculation to solve partial differential equations (PDE) into an algebraic equation that can be calculated using computer aids. The four turbine models to be simulated are shown in Figure 2.

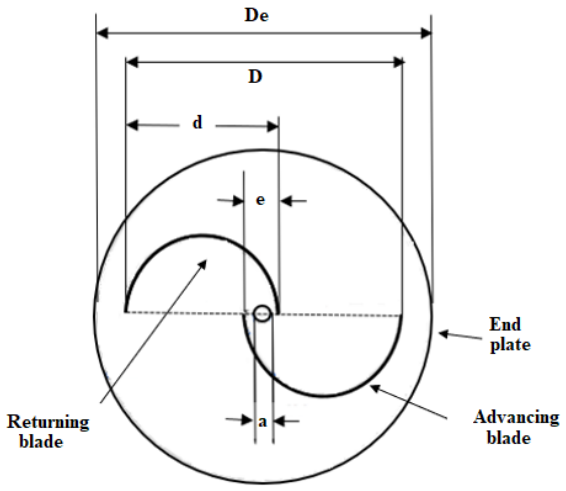

Figure 1. Geometry of classic Savonius turbine.

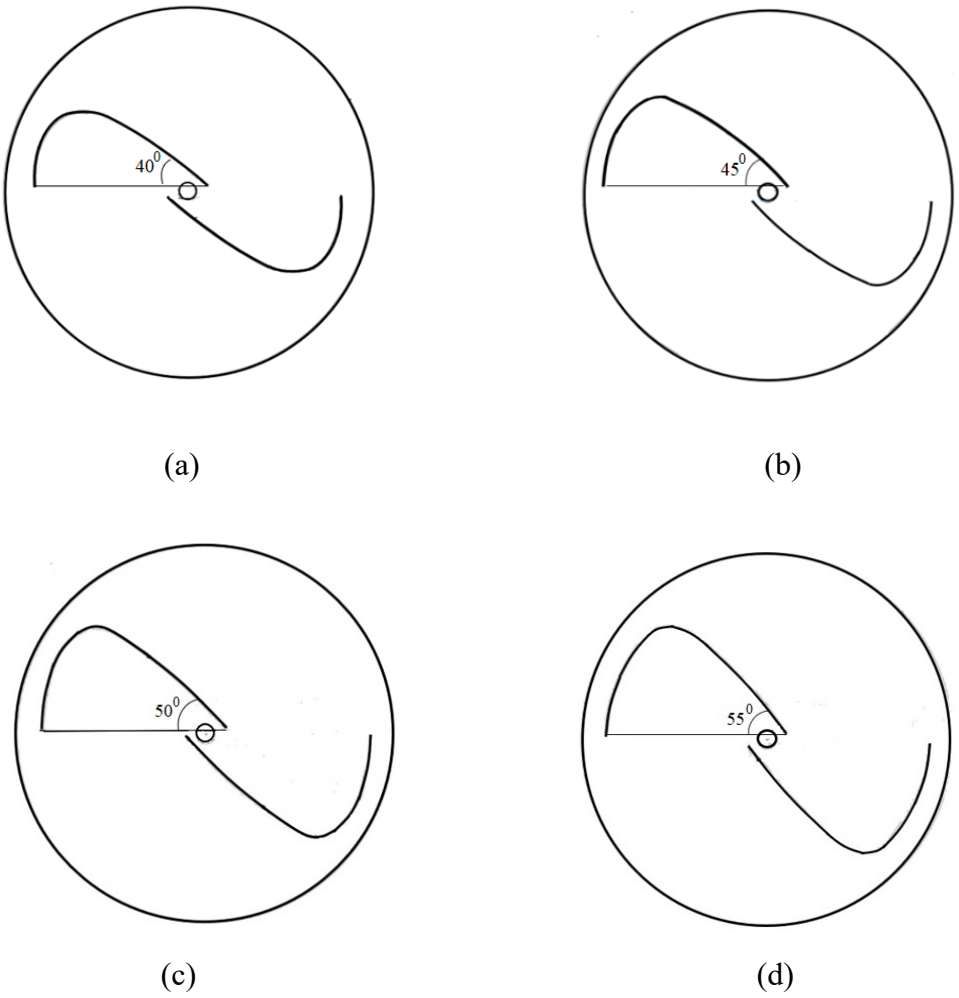

Figure 2. Elliptical-type wind turbine: (a) Base elliptical; (b) Modification I; (c) Modification II; (d) Modification III.

3.2. Computational methodology

CFD simulation has three stages that must be followed sequentially and continuously, which are divided into preprocessing, processing, and post-processing.

3.2.1. PreProcessing

Generally, the preprocessing stage must be completed in three stages: Geometry creation, domain determination and mesh or grid generation.

Geometry creation

This stage aims to create a simulation model according to what is desired. There are two types of domains that are commonly used. In this simulation, a 2D model is used according to the reference. Figure 3 shows the simulated geometric dimensions for the rotating domain.

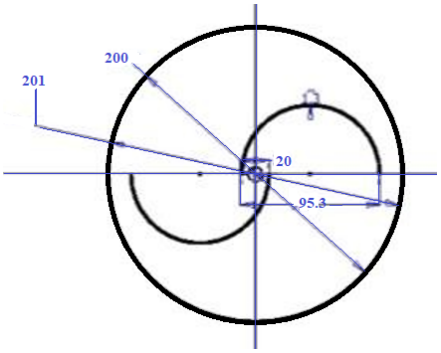

Figure 3. Simulated geometry dimensions for the rotating domain.

Determination of simulation domain

This stage determines the simulation model used, where the geometry domain is defined as a stationary fluid (enclosure) and a moving fluid (rotating) representing the vertical-axis wind turbine (VAWT). In CFD simulation, creating domains and geometry simplifies the simulation algorithm to define the simulated domain with design constraints. As shown in Figure 4, the entire computational domain is divided into two subdomains to simulate the rotating rotor. The best quality subdomain includes the rotor network component (rotating domain), and the low-resolution secondary subdomain includes cells in the outer region (stationary domain). Here, the size of the rotating cell zone relative to the turbine diameter is maintained. The inlet zone, measured from the center to the left boundary, is determined to be five times the rotor diameter. For comparison, the exit zone should be ten times the diameter of the rotor.

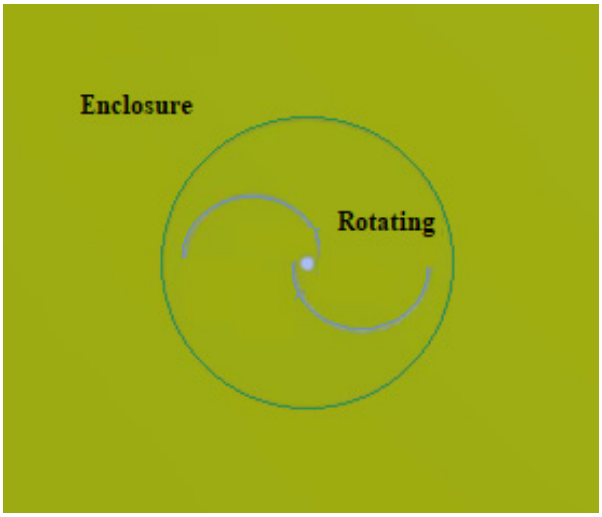

Figure 4. CFD Simulation domain model.

There are two fluid domains, including the enclosure as a fluid domain that will flow into rotating and a rotating domain that functions as a rotary for blade rotation. Figure 5 shows the area of origin of the rotating CFD simulation domain. It can be seen that there are several domains defined, including:

a. Inlet as a location for fluid entry.
b. Outlet as output.
c. Symmetry as the outermost boundary that is not walled, so there is no boundary layer.
d. Blade as a rotating wall according to the specified angular speed and the data collection point (Figure 6).

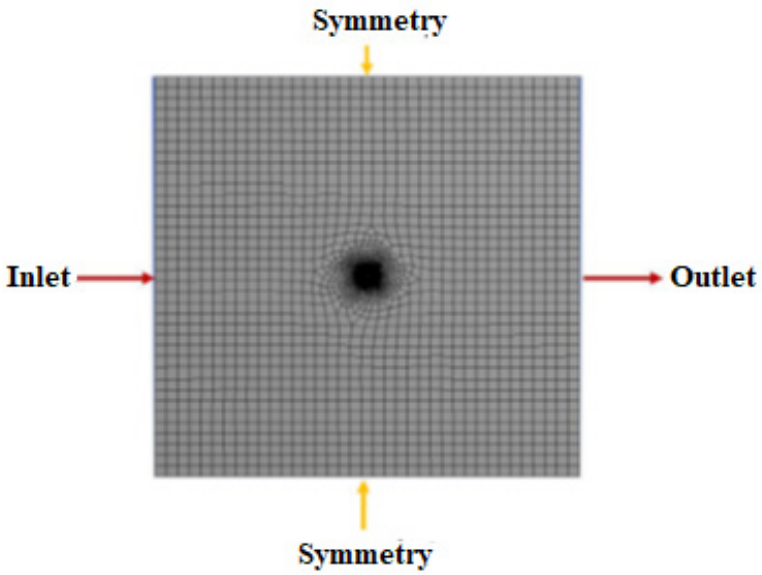

Figure 5. Domain origin area rotating.

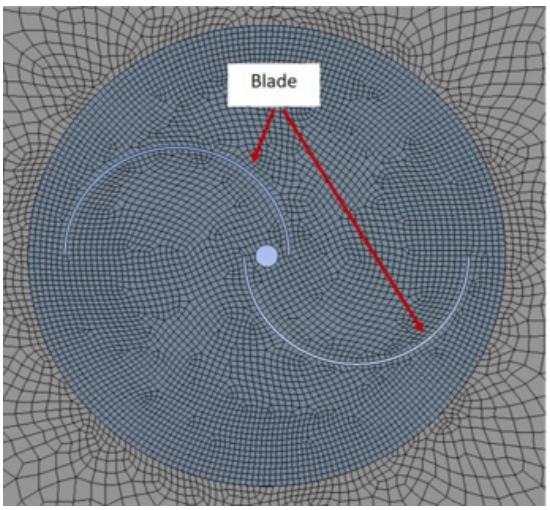

Figure 6. Mesh on blade.

Mesh generation

The mesh or grid is a model of discretization (breaking down) of a geometric model into a 2D elemental plane with a more straightforward shape. The grid stage aims to simplify discrete mathematic algorithms in analyzing simulation models based on essential shape areas, such as squares, triangles and circles. Due to the limitations of numerical algorithms, which cannot calculate complex geometric domain models, a mesh is required. According to [21], the mesh or grid method is usually used to measure unstable flow areas. Likewise, the relative motion between the fixed area and rotation area is measured using this method. Therefore, using elements from multiple dimensions in the computational domain is necessary to maintain mesh consistency. Hybrid networks are discrete in the computing domain. A triangular mesh is applied in most domains, but walls near the blades with rectangular mesh will produce good performance as shown in Figure 7.

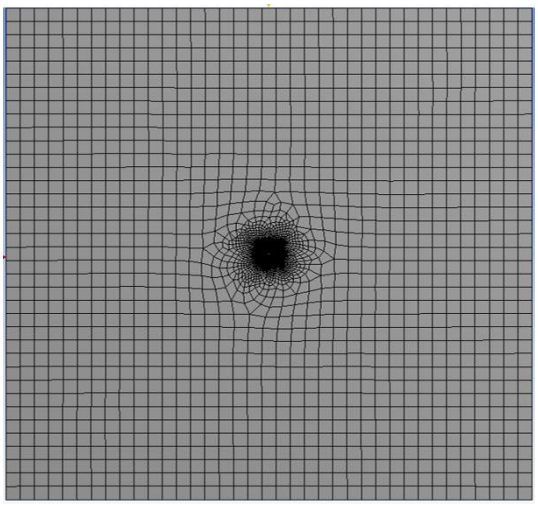

Figure 7. Mesh used in the simulation.

3.2.2. Processing (solver)

The processing stage aims to define the equation that will be used. Here, boundary conditions are defined according to the original conditions. Because the simulation model is an ideal condition, several variables are assumed to be ideal. Several stages in the solver include.

Set-up

In this stage, the aim is to understand the phenomena and physical conditions of the simulation model. Some considerations that need to be made include the following:

Compressible or incompressible flow simulation model.

Type of simulation model (ordinary fluid flow, multiphase, combustion, heat transfer, or other models).

Type of flow in simulation.

Details of the data to be processed.

Input material to be simulated.

Determination of boundary conditions.

Solutions

This stage carried out several case studies on the CFD analysis scheme. The PDE will be transformed into a set of algebraic equations depending on the space discretization scheme (finite difference or finite volume method), high/low order approximations, time discretization scheme (explicit or implicit), stability, time-step control, and convergence criteria. There are two things to consider in this processing stage: (i) time and (ii) quality of simulation results. The above arrangement, the geometry domain's size and the computational tools' capabilities will determine the simulation time. Furthermore, the quality of the simulation results depends on the following:

Mathematical models and assumptions used.

The approximation and stability of the numerical scheme.

Mesh (Grid), time discretization, and convergence criteria.

3.2.3. Post-processing

This stage is the final process of the simulation with output in the form of:

Calculate derived properties (flow function, vorticity).

Calculate integral parameters (force, total mass).

Visualization (1D data; line plots; 2D data; streamlines or contours. 3D data; isosurface, isovolumes, particle tracing, and animation).

Data Analysis (error).

Verification and validation of the CFD model.

A significant part of this stage is ensuring the model is verified and validated. The main goal of verification and validation is for the CFD code to produce reasonable results for a limited range of flow problems.

3.3. Numerical simulation

To solve the unstable Reynolds-Naiver-Stokes (URAN) equation, the ANSYS Fluent version 15 software was used. The clutch algorithm solved the pressure-based clutch pressure speed using ANSYS Fluent. The spatial discretization of the wind for the second-order algorithm is used for all pressure, momentum and turbulence equations. On the other hand, to achieve high accuracy, a gradient least squares cell-based algorithm is used. Meanwhile, a sliding mesh is used to model turbine rotation over time. The moment value (M) obtained is used to calculate the moment coefficient (C_m) as follows:

$$C_m = \frac{Pitching\ moment}{Dynamic\ moment} = \frac{M}{\frac{1}{4}\rho A_s dV_\infty^2} \tag{19}$$

where:

C_m = moment coefficient
ρ = density of air (Kg/m^3)
M = moment of force on blade (Nm)
As = swept area (m2)
A_s = velocity of air fluid (m/s)
$dV2$ = the Cp is calculated using the equation:

The Cp is calculated using the equation:

$$C_p = \frac{Rotor\ power}{Wind\ power} = \frac{Pr}{\frac{1}{2}\rho As.dV_\infty^3}, \tag{20}$$

where: $C_p = C_m \times \lambda$.

In this simulation, two main zones are planned: First, the stationary domain, which includes inlet velocity and outlet pressure. For the inlet speed, the free wind speed reaches V∞ 9 m/s in the x direction, the outlet is pressurized, and the walls are symmetrical. Second, the rotating domain includes turbine blades with counterclockwise rotation according to the time step. The time step for all 2D simulations was set to 274-time steps per rotation. The rotational speed of the domain depends on the turbine based on the velocity angle and can be calculated by TSR (λ). It is defined as the linear velocity of the blade tip concerning the undisturbed flow velocity using Eq 21. Table 3 shows the varying tip speed ratios to angular velocity.

$$\lambda = \frac{\omega R}{v\infty} \tag{21}$$

Table 3. Tip speed ratio λ angular velocity ω.

λ	0.5	0.6	0.7	0.8	0.9	1
ω (Rad/s)	45	54	63	72	81	90

4. Results

4.1. Flow field analysis

In this paper, a comparison of the classic turbine with the elliptical turbine and three modifications has been carried out. The base angle of the elliptical turbine is made at 40°, then, the turbine blade angle is changed to 45°, 50° and 55°, as shown in Figure 2, and 3D simulations are carried out to visualize and analyze the flow field around the optimal elliptical bladed rotor at a tip speed ratio of 0.7 and 0.8. Figure 8 shows the classic Savonius pressure contours with TSR 0.7 and 0.8 for the basic elliptical blade design (40°) and its modifications at three different positions of 45°, 50° and 55°. The pressure contour shows that the classical Savonius turbine produces less than the elliptical turbine. Furthermore, it can be seen that the elliptical turbine modification obtained the highest pressure at position 45° for TSR 0.7 and 55° for TSR 0.8. Due to the higher-pressure difference on the modified blade, the resulting wake is smaller than on a conventional blade. The contour plot shows the pressure difference between upstream and downstream around the rotor. Red areas on the bar indicate higher pressure rises, while blue areas indicate lower pressure. The pressure increase on modified elliptical blades is relatively more significant than on blades with an elliptical-base because the blade shape is more circular. In contrast, blades with an elliptical base only have a circular shape at the blade's tip. This shape optimization differentiates the 45°, 50° and 55° modification blades from standard elliptical blades.

On the convex side of the two blades, static pressure can be seen under the concave side of the blade. However, in reality, there is negative pressure on the convex side of the blade due to the high flow velocity at the convex end of the blade. Therefore, a pressure difference between the convex and concave sides of the blade produces the torque required to rotate the blade.

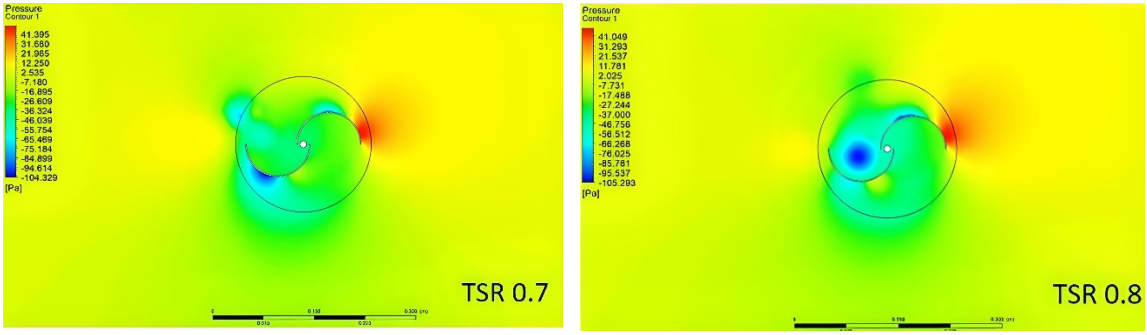

a

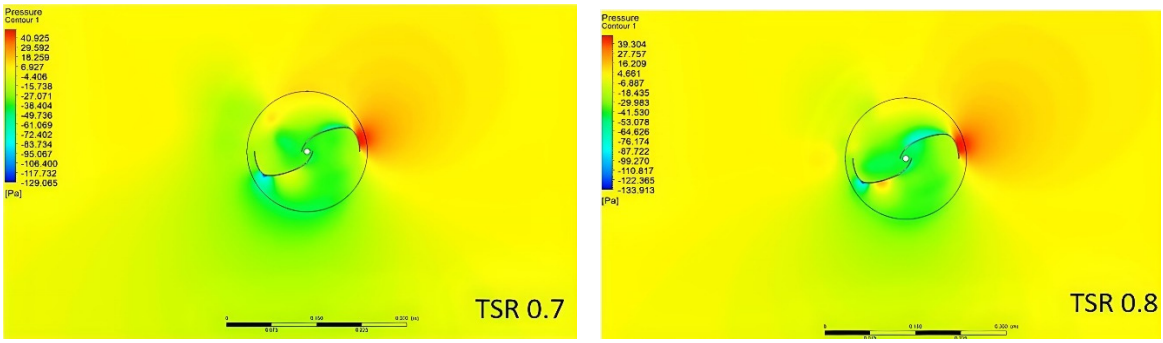

b

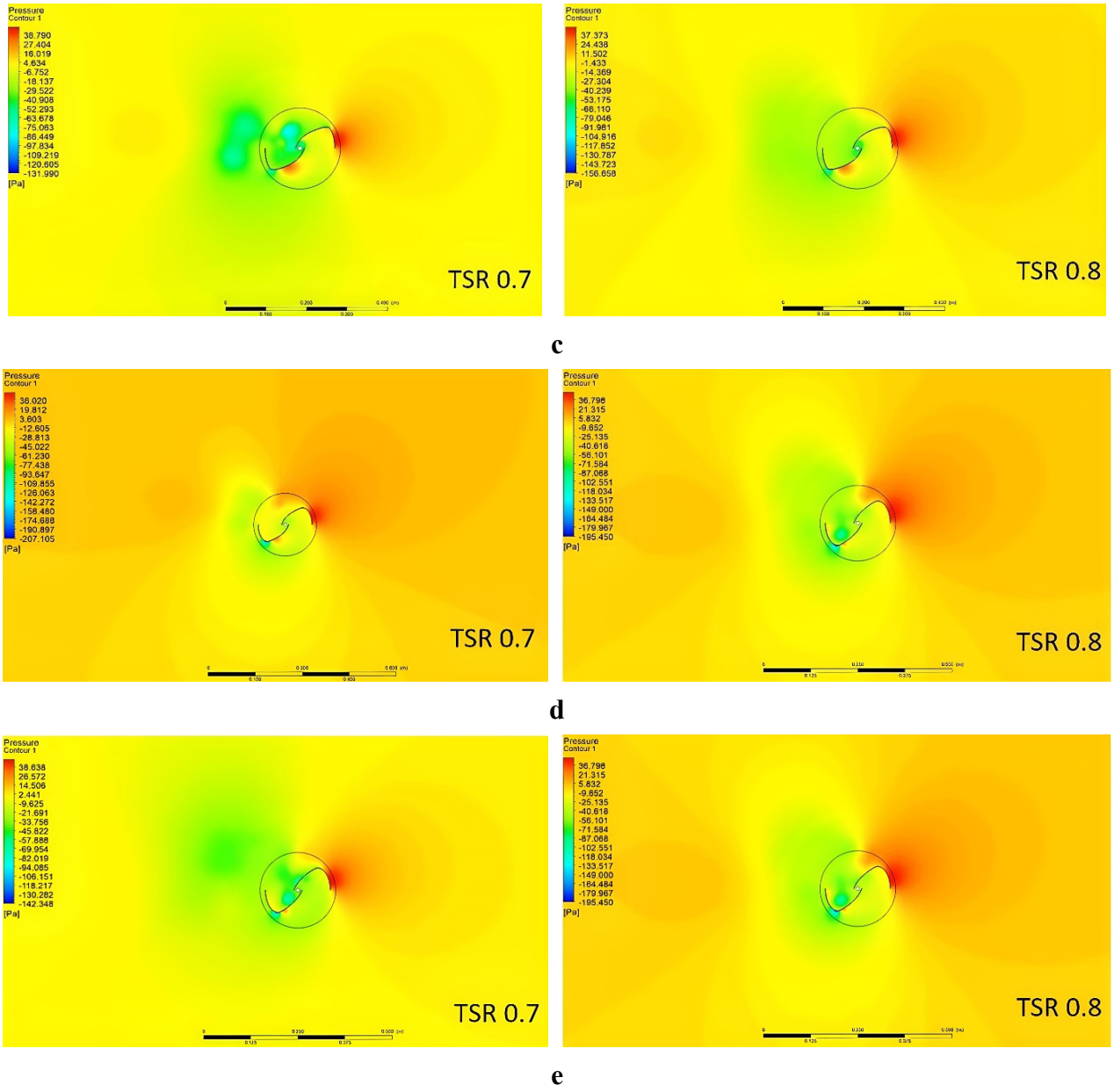

Figure 8. Comparison of pressure contours between conventional Savonius blades and elliptical blades and their modifications at TSR 0.7 and 0.8 (a) Classic Savonius (b) Elliptical base blades (40°) (c) Modification 1 (45°) (d) Modification 2 (50°) (e) Modification 3 (55°).

4.2. Pitching moments

Figure 9 compares each blade model's pitching moment (PM) and the TSR. The figure shows that the pitching moment decreases as the TSR increases. That is reasonable because, theoretically, a turbine that rotates at a low speed (small TSR) absorbs more wind energy. In contrast, the turbine rotates at a high speed (large TSR), and the wind energy that the turbine can absorb is minimal. In this case, what needs to be considered is which blade model can absorb wind energy better at both small and large TSR values. Of the five-blade models tested at a speed of nine m/s, including the conventional model, the basic elliptical model, and its modifications, it turned out that the second modification was the most optimal in absorbing wind energy. The high pitching moment value between conventional blades and the first and third modified elliptical blades indicates this. In the TSR range of 0.5 to 1.0, the average pitching moment for conventional blades is 0.03–0.02. Average pitching moments of 0.03–0.026 for the basic elliptical, 0.9–0.59 for the first modification, 1.46–0.8 for the second modification, and 1.39–0.48 for the third modification were successfully obtained.

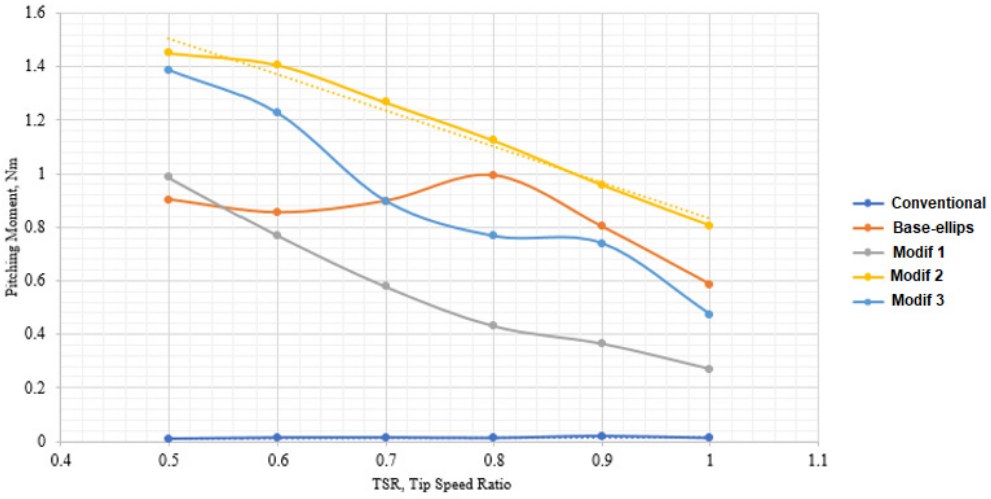

Figure 9. Comparison of the moment coefficients of the five blade models.

4.3. Power coefficient

By multiplying the throwing moment by the TSR, the Cp is obtained. Figure 10 compares the Cp and TSR for each blade model. It can be seen that the second modified elliptical blade (50°) has the highest Cp of 0.59 compared to the other blades. This experiment was carried out at a speed of 9 m/s. In contrast, the lowest is the first modified blade model (45°). Therefore, modifying the second elliptical turbine with a 50° angle allows the turbine to spin higher and produce more power as the graph trends, maintaining Cp at a higher TSR. This is very useful if this wind turbine model is applied to locations where wind speeds reach nine m/s. That has also been proven in tests with speeds varying between 5–12 m/s, as seen in Figure 9. At a speed of 9 m/s, the second modified blade produces the highest CP value (Yellow Line) among the other blades. Considering the CP value, the second elliptical turbine modification is the right choice.

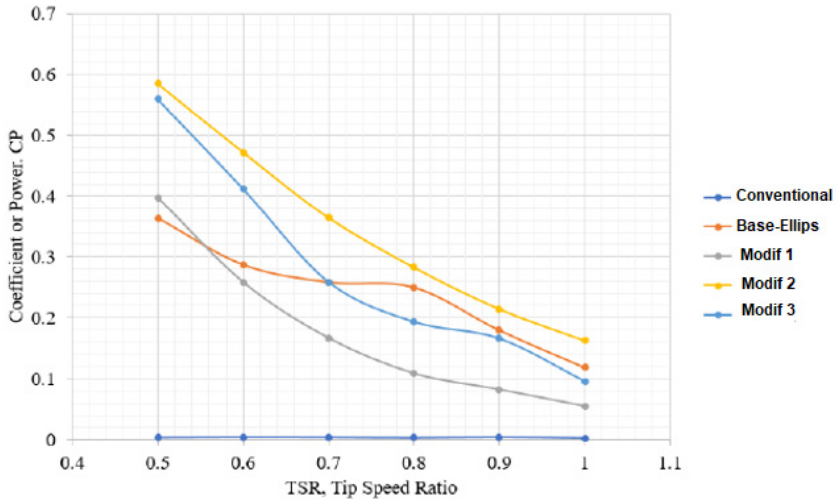

Figure 10. CP vs TSR.

However, it is different if the wind speed is above 9–12 m/s. The second modified blade cannot withstand wind pressure above 9–12 m/s, as seen in Figure 11. It can be seen that the basic blade elliptical is only able to withstand wind pressure at a speed of 6–10 m/s. On the other hand, the elliptical blades of the first and third modifications are stable and tend to increase wind speed by 5–12 m/s. In particular, the third modification has a higher CP than the first modification, making it suitable for varying speeds. The same thing can also be seen in the pitching moment of the fifth blade model, as seen in Figure 12. The stability of the pitching moment in the third blade modification is also seen at speeds of 5–12 m/s.

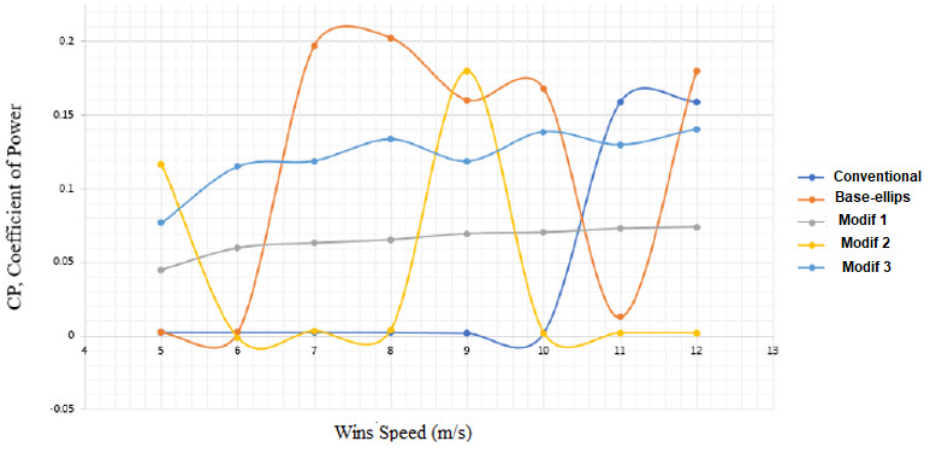

Figure 11. CP vs wind speed.

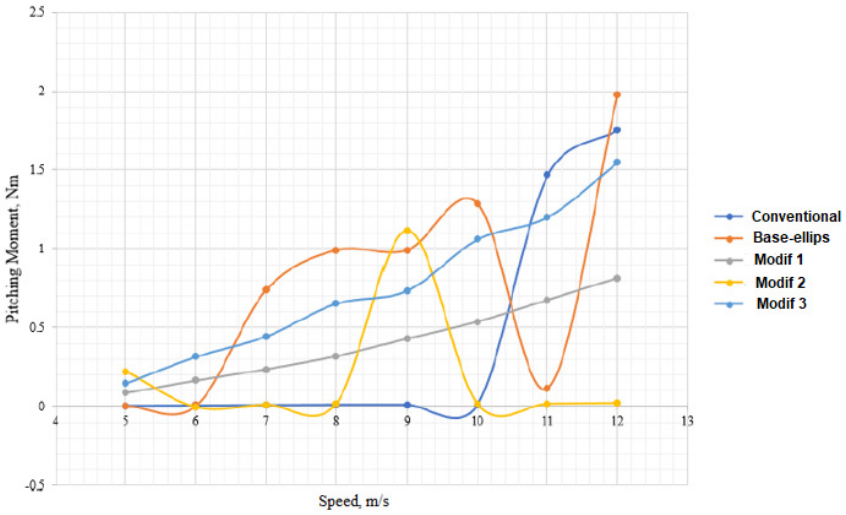

Figure 12. Pitching moments of various speed variations.

5. Discussion

The development of the Savonius turbine in the future is expected to compete with the horizontal-axis wind turbine (HAWT) type, which has been widely used in wind power plants. Although the Savonius is now dominated by the VAWT type with a more straightforward construction than the horizontal type, some researchers are still investigating their performance comparisons. In the paper, Pope et al. [28] investigated and compared the performance of horizontal and VAWTs. The results obtained show that there is a significant difference where the power coefficient of the HAWT type (0.44) is higher than the vertical type, which consists of Savonius (0.18) and Zephyr (0.11). On the other hand, in terms of the static and dynamic response, the VAWT type generates very different aerodynamic forces on the supporting structure, notably potentially lower tipping moments and much higher torques than HAWT [29].

The Savonius style wind turbine is a class of VAWTs, apparently promising for rural applications. Some advantages include simple design, good starting ability, insensitivity to wind direction, relatively low operating speed, low cost, and easy installation. This work is intended to discuss the factors of changes in the influence of the axis angle effect of the modified elliptical Savonius turbine to improve its performance in harvesting wind energy. In [24], an elliptical blade profile with an angle of 47.5° has demonstrated its potential to harness wind energy more efficiently. The tests were carried out at wind speeds of up to 9 m/s. The same has been achieved in this paper. Testing modification two with an axis angle of 50° has the highest CP among other elliptical blade modifications. However, modified elliptical blades with an axis angle of 50° cannot withstand wind speeds above nine m/s. On the other hand, a modified elliptical blade with an axis angle of 40° and a modified blade three with an angle of 55° show the ability to stabilize pressure at wind speeds above 9–12 m/s. Even though the standard elliptical blade has the highest CP compared to the other blades, there is a tendency to decrease/fluctuate at wind speeds of 10 m/s. In addition, modification three is stable and tends to increase CP up to wind speeds of 12 m/s. This finding reinforces previous research that elliptical turbines with angles above 45° can increase the power coefficient compared to the classic Savonius and standard elliptical turbines.

On the other hand, several references have investigated the lower torque ratio of classical turbines compared to elliptical turbines [20,22,23]. However, the investigation was conducted in wind

conditions with a top speed of up to 9 m/s. Another finding in this paper is that the CP capability of conventional turbines increases at wind speeds above 10 m/s (Figure 11). It indicates that conventional Savonius turbines can be applied and perform better in areas with medium and high wind speeds. Meanwhile, standard elliptical turbines are suitable for use in areas with low wind speeds.

6. Conclusions

Modifying an elliptical blade with an axis angle of 50° with TSR variation conditions is the best design with the largest CP. It has the most significant pitching moment, with a constant velocity condition of 9 m/s.

The best design with the largest CP with speed variations ranging from 5–12 m/s was obtained for the first and third modified elliptical blades because they had the most significant pitching moment with a persistent TSR condition of 0.8. The blade design with an axis angle of 55° (third modification) is suitable for a wide range of speeds.

Compared with the elliptical blade model and variations in axis angles, the classical turbine has a CP that increases at wind speeds above 10 m/s, which is suitable for application at this wind speed.

Acknowledgments

The authors would like to acknowledge the Laboratory of Electrical Engineering and the for funding University of Nusa Cendana-Kupang, as well as the Ministry of Research and Technology this research in the Higher Education Excellence Applied Research Grant with contract number 152/UN15.19/SP2H/LT/2022.

Use of AI tools declaration

The authors declare that they have not used Artificial Intelligence (AI) tools in the creation of this article.

Conflict of interest

All authors declare no conflict of interests in this paper.

References

1. Alom N, Borah B, Saha UK (2018) An insight into the drag and lift characteristics of modified bach and benesh profiles of Savonius rotor. *Energy Proc* 144: 50–56. https://doi.org/10.1016/j.egypro.2018.06.007
2. Khammas FA, Hussein Suffer K, Usubamatov R, et al. (2015) Overview of vertical axis wind turbine (VAWT) is one of the wind energy application. *Appl Mech Materials* 793: 388–392. https://doi.org/10.4028/www.scientific.net/amm. 793.388
3. Attar AE, Shahin A (2018) Vertical axis wind turbine. Bachelor Thesis. https://doi.org/10.13140/RG.2.2.12592.81927

4. Zemamou M, Aggour M, Toumi A (2017) Review of Savonius wind turbine design and performance. *Energy Proc* 141: 383–388. https://doi.org/10.1016/j.egypro.2017.11.047
5. Sun X, Chen Y, Cao Y, et al. (2016) Research on the aerodynamic characteristics of a lift drag hybrid vertical axis wind turbine. *Adv Mech Eng* 8: 1–11. https://doi.org/10.1177/1687814016629349
6. Pranta MH, Rabbi MS, Roshid MM (2021) A computational study on the aerodynamic performance of modified Savonius wind turbine. *Results Eng* 10: 100237. https://doi.org/10.1016/j.rineng.2021.100237
7. Wafula D, Otieno C, Ngugi J (2020) An experimental investigation into performance characteristics of H-shaped and Savonius-type VAWT rotors. *Sci African* 10: e00603. https://doi.org/10.1016/j.sciaf.2020.e00603
8. Latif M (2013) Savonius turbine prototype efficiency at low wind speeds. *J Rekayasa Elekt* 10: 147–152. https://doi.org/10.17529/jre.v10i3.1030
9. Saha UK, Thotla S, Maity D (2008) Optimum design configuration of Savonius rotor through wind tunnel experiments. *J Wind Eng Ind Aerodyn* 96: 1359–1375. https://doi.org/10.1016/j.jweia.2008.03.005
10. Wenehenubun F, Saputra A, Sutanto H (2015) An experimental study on the performance of Savonius wind turbines related with the number of blades. *Energy Proc* 68: 297–304. https://doi.org/10.1016/j.egypro.2015.03.259
11. Hadi AM (2013) Experimental comparison study for Savonius wind turbine of two & three blades at low wind speed. *Int J Modern Eng Res (IJMER)* 3: 2978–2986.
12. Mao Z, Tian W (2015) Effect of the blade arc angle on the performance of a Savonius wind turbine. *Adv Mech Eng* 7: 1–10. https://doi.org/10.1177/1687814015584247
13. Mahmoud NH (2012) An experimental study on improvement of Savonius rotor performance. *Alexandria Eng J* 51: 19–25. https://doi.org/10.1016/j.aej.2012.07.003
14. Mahmoodaslam M, Uzairfarooqzainalish B (2012) Vertical axis wind turbine—A review of various configurations and design techniques. *Renewable Sustainable Energy Rev* 16: 1926–1939. https://doi.org/10.1016/j.rser.2011.12.004
15. Olaoye OS, Adeoye O (2016) Numerical investigation and improvement of aerodynamic performance of Savonius wind turbine. *J Energy Tech Policy* 6: 34–43.
16. Kamoji MA, Kedare S, Prabhu SV (2009) Experimental investigations on single stage modified Savonius rotor. *Appl Energy* 86: 1064–1073. https://doi.org/10.1016/j. apenergy.2008.09.019
17. Prabowo AR, Prabowoputra DM (2020) Investigation on Savonius turbine technology as harvesting instrument of non-fossil energy: Technical development and potential implementation. *Theoretical Appl Mech Letters* 10: 262–269. https://doi.org/10.1016/j.taml.2020.01.034
18. Lee JH, Lee YT, Lim HC (2016) Effect of twist angle on the performance of Savonius wind turbine. *Renewable Energy* 89: 231–244. https://doi.org/10.1016/j.renene.2015.12.012
19. Anwar K, Himran S, Sule L, et al. (2018) Numerical investigation of modified Savonius wind turbine with various straight blade angle. *J Mech Eng Res Dev* 41: 38–42. https://doi.org/10.26480/jmerd.03.2018.38.42
20. Banerjee A, Sukanta R, Mukherjee P (2015) Unsteady flow analysis around an elliptic-bladed Savonius-style wind turbine. *ASME 2014 Gas Turbine India Conference*, New Delhi, India, 1–7. https://doi.org/10.1115/GTINDIA2014-8141

21. Hashem I, Mohamed MH (2018) Aerodynamic performance enhancements of H-rotor darrieus wind turbine. *Energy* 142: 531–545. https://doi.org/10.1016/j.energy.2017.10.036
22. Kacprzak K, Liskiewicz G, Sobczak K (2013) Numerical investigation of conventional and modified Savonius wind turbines. *Renewable Energy* 60: 578–585. https://doi.org/10.1016/j.renene.2013.06.009
23. Talukdar PK, Kulkarni V (2021) Aerodynamic performance characterization of a drag-based elliptical-bladed Savonius wind turbine rotor. *ASME 2021 Gas Turbine India Conference*, 164766. https://doi.org/10.1115/GTINDIA2021-76001
24. Alom N, Kolaparthi SC, Gadde SC, et al. (2016) Aerodynamic design optimization of elliptical-bladed Savonius-style wind turbine by numerical simulations. *ASME 2016 35th International Conference on Ocean, Offshore and Arctic Engineering*, Busan, South Korea, 6. https://doi.org/10.1115/OMAE2016-55095
25. Jiao X, Yang Q, Xu B (2021) Hybrid intelligent feedforward-feedback pitch control for VSWT with predicted wind speed. *IEEE Trans Energy Convers* 36: 2770–2781. https://doi.org/10.1109/TEC.2021.3076839
26. Meng WC, Yang QM, Ying YX, et al. (2015) Adaptive control of variable-speed wind energy conversion systems with inaccurate wind speed measurement. *Trans Inst Meas Control* 37: 63–72. https://doi.org/10.1177/0142331214531008
27. Launder BE, Sharma BI (1974) Application of the energy-dissipation model of turbulence to the calculation of flow near a spinning disc. *Letters Heat Mass Transf* 1: 131–137. https://doi.org/10.1016/0094-4548(74)90150-7
28. Pope K, Dincer I, Naterer GF (2010) Energy and exergy efficiency comparison of horizontal and vertical axis wind turbines. *Renewable Energy* 35: 2102–2113. https://doi.org/10.1016/j.renene.2010.02.013
29. Borg M, Collu M (2015) A comparison between the dynamics of horizontal and vertical axis offshore floating wind turbines. *Phil Trans R Soc A: Math Phys Eng Sci* 373: 20140076. https://doi.org/10.1098/rsta.2014.0076

AIMS Press